Soft Matter

PAPER

View Article Online
View Journal | View Issue

Cite this: *Soft Matter*, 2020, **16**, 9306

Mechanical basis for fibrillar bundle morphology†

Thomas C. T. Michaels,[a] Edvin Memet[b] and L. Mahadevan*[abc]

Received 22nd June 2020,
Accepted 18th August 2020

DOI: 10.1039/d0sm01145b

rsc.li/soft-matter-journal

Understanding the morphology of self-assembled fibrillar bundles and aggregates is relevant to a range of problems in molecular biology, supramolecular chemistry and materials science. Here, we propose a coarse-grained approach that averages over specific molecular details and yields an effective mechanical theory for the spatial complexity of self-assembling fibrillar structures that arises due to the competing effects of (the bending and twisting) elasticity of individual filaments and the adhesive interactions between them. We show that our theoretical framework accounting for this allows us to capture a number of diverse fibril morphologies observed in natural and synthetic systems, ranging from Filopodia to multi-walled carbon nanotubes, and leads to a phase diagram of possible fibril shapes. We also show how the extreme sensitivity of these morphologies can lead to spatially chaotic structures. Together, these results suggest a common mechanical basis for mesoscale fibril morphology as a function of the nanoscale mechanical properties of its filamentous constituents.

1 Introduction

Fibrillar aggregates are ordered bundles composed of several filaments wound around each other and held together by adhesive forces. Such structures represent one of the simplest geometrical examples of supramolecular self-assembly[1] and are ubiquitous both in living and synthetic systems. In living cells, fibrillar structures provide structural rigidity, serve as locomotory appendages, and guide cell division;[2] examples include actin filaments, tubulin microtubules, the bacterial flagellum, aggregates of the protein fibrin,[3] or actin microchaetes.[4] Fibrillar aggregates are found also in the context of disease, such as in the case of misfolded proteins that form amyloid fibrils linked to Alzheimer's and Parkinson's diseases[5,6] or sickle cell anaemia.[7,8] Finally, fibrillar bundles find widespread use in modern materials science for various technological applications, either as protein-based materials[9,10] or as inorganic nanotubes.[11,12]

Two central questions arising from the self-assembled nature of fibrillar bundles are (i) understanding the mechanical basis for morphology selection in natural living systems and (ii) learning how to achieve precise control of fibrillar structures at the scale of the aggregate, a key challenge of current nanotechnology.[13–15] The ability to aggregate into fibrillar structures is common to a large number of peptides, proteins and synthetic building blocks with very different chemical composition.[16] Notably, fibrillar bundles are characterised by persistence lengths between 10–100 μm (*e.g.* haemoglobin fibrils,[8] actin bundle in *Limulus* sperm[17]), which are orders of magnitude larger than the typical sizes of the bundles themselves. This implies that self-assembled structures have well-defined shapes that are not affected significantly by thermal fluctuations. Taken together, these observations raise the natural question of whether we can go beyond the specific molecular details that distinguish such systems to provide a unifying generic mechanical model for the spatial complexity of the morphology of fibrillar assemblies.

Motivated by this underlying question of morphology selection, an emerging central theme in this area is geometric frustration, the idea that locally preferred packing motifs may be incompatible with global order constraints in the assembly. This mismatch between local and global order yields non trivial bundle shapes, and was already recognized in the early work by Makowski and coworkers,[18,19] and later extended to account for inter-filament stretch,[8] orientational gradients,[20–22] variable inter-filament spacing,[23] inter-filament shearing[24–26] *etc.* More recently, both continuum approaches using the formalism of liquid crystals[8,20–29] and coarse-grained computer simulations[13] have focused on the role of frustration-induced chirality to study these assemblies, summarized and reviewed in ref. 14 and 15. Recently these models have been extended also to achiral systems with spontaneous twist, highlighting that chirality is not necessary to yield frustration.[28] These studies show that under general

[a] *Paulson School of Engineering and Applied Sciences, Harvard University, Cambridge, MA 02138, USA*
[b] *Department of Physics, Harvard University, Cambridge, MA 02138, USA*
[c] *Department of Organismic and Evolutionary Biology, Harvard University, Cambridge, MA 02138, USA. E-mail: lmahadev@g.harvard.edu*

† Electronic supplementary information (ESI) available: Video S1: Simulation of interacting discrete filaments and their emerging morphology for parameters $\gamma = 0.07$, $B = 1$, $a = 1.5$, $\theta(0) = 0$, $\dot{\theta}(0) = 0.3$ in a 2D setting with φ,ψ = const. Video S2: Simulation of interacting discrete filaments and their emerging morphology for parameters $\gamma = 0.01$, $B = 1$, $a = 1.5$, $\theta(0) = 0.6$, $\dot{\varphi}(0) = 0.3$ in a 3D setting with θ,ψ = const. See DOI: 10.1039/d0sm01145b

conditions frustration can yield to fibril structures with finite diameter, but have focussed mainly on straight bundle structures. Understanding the range of large-scale morphologies of non-straight fibril bundles that emerge from the small-scale properties of the constituent monomers remains an open question.

In this paper we take a step forward in this direction by proposing an effective theory predicated on the hypothesis that complex spatial fibril configurations can emerge from just two simple and natural physical ingredients: the competition between three-dimensional bending and twisting of the filaments that constitute the fibril (and thus the bending and twisting of the fibril itself) and the adhesive interactions between the filaments in the fibrillar bundle. Using a combination of continuum theory and coarse-grained simulations we explore systematically the range of fibril bundle shapes that emerge from the mismatch between local packing due to inter-filament adhesion and global constraints imposed by collective bundle bending and twist. We show that our model, which is simple in its assumptions but broad in its scope, can account for a variety of forms observed in a number of natural and synthetic systems as diverse as *Filopodia* and multi-walled carbon nanotubes.[17,30–32] Finally we exploit a direct analogy between our mechanical model and the complex motion in time of a rigid body in an external potential[33–35] to predict, that the resulting morphology of three-dimensional fibrillar bundles can be spatially chaotic.

2 Mesoscopic models for fibrillar bundles

Our starting point is the idea that the mesoscopic scale morphology of fibrillar bundles can be captured in terms of a few important coarse-grained parameters,[13,23,36–43] including long-wavelength elastic deformations and the strength of the adhesive forces that keep the filaments in the bundle together. Morphology arises *via* a dynamical process that involves addition of monomer material to the ends of fibrils followed by equilibration of elastic energy. However, there is a separation of time scales between the slower growth of bundles *via* addition of monomers and the relatively rapid equilibration of elastic energy. An upper bound for the equilibration time of elastic energy is obtained by considering the bending motion of a long filamentous object of length L, radius r with aspect ratio $L/r \simeq 100$ and Young's modulus $E \simeq 10$ GPa in a liquid medium with viscosity $\eta \simeq 10^{-3}$ N s m^{-2}; balancing the bending torque Er^4/L with the viscous torque $\eta L^3/\tau_{el}$ gives $\tau_{el} \simeq (\eta/E)(L/r)^4 \simeq 10$ μs. At low monomer concentrations c, diffusion limits the rate at which monomers can add to fibrils. For a typical concentration $c \simeq 1$ μM, the timescale for diffusion into an effective reaction volume of linear dimension $r_{eff} \simeq 1$ nm is estimated as $\tau_D \simeq (Dcr_{eff})^{-1} \simeq 1$ ms, where $D \simeq 10^{-10}$ m^2 s^{-1} is a typical diffusion coefficient for monomers.[44] Since $\tau_{el} \ll \tau_D$, we can treat the shaping of the fibrils as an equilibrium problem, where the total elastic energy of bending/twisting and adhesion is minimised after each monomer addition event to yield the equilibrium fibril shape (see Videos S1 and S2, ESI†).

2.1 Simulations of interacting discrete filaments

As a first attempt to understand the morphology of fibrils, we devised a computer simulation model of discrete adhering filaments to provide a baseline against which to compare our effective coarse-grained theory (Fig. 1 and Appendix A). Simulations are carried out using Espresso, a coarse-grained molecular dynamics software.[45] In our model it is sufficient to consider the interaction of two filaments, each composed of spherical monomers spaced a distance a apart ($2r_0 \leq a < 4r_0$), where a sets the corrugation length scale. For simplicity we focus here on monomers with spherical symmetry, but note that this model could be extended to account for asymmetry and chirality in monomer interactions. Monomers on distinct filaments interact through a Lennard-Jones (L-J) potential with equilibrium distance r_0 and well depth γ (Fig. 1(a)). Monomers on the same filament are connected by springs of rest length a (Fig. 1(a), top) and very large stiffness k (modeling inextensibility), while triplets of neighbouring monomers determine a bending interaction (see Methods). We describe the configuration of the filament by using the Euler angles θ, φ and ψ, defined in Fig. 2(b). In a simplified two-dimensional setting with constant φ and ψ, the bending interaction takes the form $B_1/a[1 - \cos(\theta - \theta_0)] \approx B_1/(2a)(\theta - \theta_0)^2$, where B_1 is the bending rigidity of the filament, θ is the (smaller) angle determined by the segment joining the three consecutive monomers (Fig. 1(a), bottom), θ_0 is related to the intrinsic curvature κ_0 of the monomer/filament ($\theta_0 = \pi - \kappa_0 a$), and $\dot{\theta} = (\theta - \theta_0)/a$ is the local curvature. We grow the filament by adding a pair of monomers at a time, starting from an initial seed region and allowing the structure to relax to its equilibrium shape at each step (see Methods and Videos S1 and S2, ESI†), consistent with our scaling estimates above.

Fig. 1(b) shows some representative simulations of 2D fibrils. The case $\dot{\theta} = 0$, with initial conditions $\theta(0) = 0$ and $\dot{\theta}(0) = 0$ corresponds to the solution $\theta(s) = 0$ for the tangent vector of the filament, where s is the arc-length parameter along the fibril: the filaments start and remain in register in the absence of any bending (Fig. 1(b)(i)). If adhesive interactions are weak, the energy density is from bending alone $B_1\dot{\theta}^2/2$, with solution $\theta(s) = \kappa_0 s$ for initial conditions $\theta(0) = 0$ and $\dot{\theta}(0) = \kappa_0$, where κ_0 represents the intrinsic curvature of monomers. Thus, a growing filament composed of monomers with intrinsic curvature grows into a circular morphology when adhesive interactions are very weak (Fig. 1(b)(ii)). However, in the presence of stronger adhesive interactions, the penalty associated with monomer mismatch drives the formation of a number of kinked-defects (Fig. 1(b)(iii)). The frequency of kinks is determined by the parameter $\chi = 2\pi d/a \approx 4\pi r_0/a$ (*e.g.* $a = 3r_0$ corresponds to $\chi \approx 4$, which results in 4 kinks, as in Fig. 1(c), inset (ii)). Varying χ through adjusting a changes the number of kinks appropriately (Fig. 1(c), inset (iii)).

Our simulations suggest that the Lennard-Jones interaction between monomers on different filaments is periodic and can be reduced to a simpler effective potential $\mathscr{H}_{adh}$ with two parameters: χ controlling periodicity, and γ controlling amplitude. To show this, we determined the adhesive potential along the

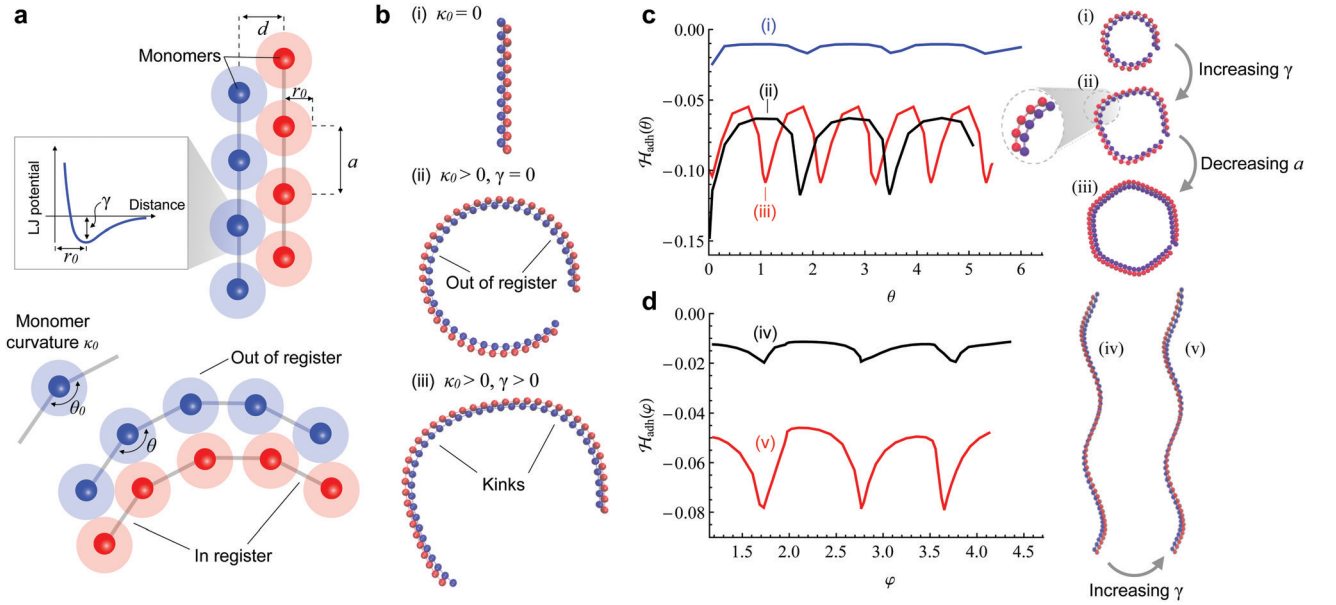

Fig. 1 Computer simulation model of adhering filaments. (a) (top): Two filaments, composed of monomers of size r_0 spaced a distance a apart, interact through a Lennard-Jones potential with equilibrium distance r_0 (which sets the monomer size) and well depth γ (inset). The interaction takes place only between monomers on different filaments while momoners on the same filament are kept apart through springs with high stiffness k and equilibrium length a. (bottom): More generally, monomers may also have an intrinsic curvature κ_0 (equivalently characterised through an equilibrium angle $\theta_0 = \pi - \kappa_0 a$ formed by triplets of neighbouring particles (inset)). Deregistration will naturally occur in two filaments spaced apart by some distance d that are trying to maintain the same curvature. (b) Filaments starting in register ($\theta(0) = 0$) composed of monomers with no intrinsic curvature ($\kappa_0 = 0$) can maintain registration indefinitely (i). Filaments composed of monomers with intrinsic curvature κ_0 tend to attain a circular morphology when the adhesion energy is sufficiently low (ii). The fibrillar structure develops kinks when adhesive interactions are sufficiently large to penalise monomer mismatch (iii). (c) Shapes of fibrillar bundles obtained *via* our computer simulation model and measurement of the associated adhesion potential (red) as a function of the angle θ (see Fig. 2(b)), keeping the other Euler angles constant. The adhesion potential changes as expected when the distance between monomers is decreased by a factor of 2/3 (black (ii) to red (i)) and when the adhesion strength γ_1 is decreased six fold (black (ii) to blue (iii)). (d) Adhesion potential as a function of the angle φ (see Fig. 2(b)) while keeping the other Euler angles constant. Increasing the strength of monomer–monomer interaction by a factor of 4 (blue (iv) to red (v)) yields a change in the strength of adhesion γ by the same factor.

filament by integrating the L-J potential (see Appendix A) to determine its form as a function of the Euler angles θ and φ. Fig. 1(c) illustrates this dependence on θ in a 2D setting with $\varphi, \psi =$ const while Fig. 1(d) illustrates the φ dependence for $\theta, \psi =$ const in a 3D setting. The coarse-grained interaction parameters γ and χ can be controlled through the parameters associated with the "microscopic" Lennard-Jones interaction which control the well depth and equilibrium distance, and the fibril geometry which controls the spacing between monomers. The data in Fig. 1(c) and (d) show that the adhesion potential is a periodic function of the Euler angles θ and φ, *i.e.* $\mathscr{H}_{adh}[\chi(\theta + 2\pi)] = \mathscr{H}_{adh}[\chi\theta]$, respectively, $\mathscr{H}_{adh}[\chi(\varphi + 2\pi)] = \mathscr{H}_{adh}[\chi\varphi]$. Moreover, the adhesion potential is proportional to the interaction strength between monomers, $V \sim \gamma$. Indeed, increasing the strength of the interactions between the monomers increases the effective potential proportionally, while increasing the distance between monomers a yields an effective adhesion potential with smaller periodicity χ (Fig. 1(c and d)).

2.2 Coarse-grained continuum theory

These results allow us to transition to a continuum rod model to capture the interplay between bending/twisting elasticity and inter-filament adhesion that emerges from our discrete rod simulations (Fig. 2(a)). A natural strategy for constructing a generalised rod theory for adhering fibrils is to consider the mechanics of curved and twisted rods in SO(3) coupled with a periodic potential for filament adhesion.

2.2.1 Bending and twisting elasticity. To capture the long-wavelength elastic deformations of the fibril, we model the bundle as an effective elastic rod of homogeneous cross section that is easy to bend and twist, but hard to stretch or shear.‡ [46,47] The spatial configuration of the fibril is then specified by a local body coordinate system $\{d_1(s),d_2(s),d_3(s)\}$ assigned to every point $s \in [0,L]$ along the center line $r(s)$, with s being the arc-length. The vector $d_3(s) = \mathrm{d}r(s)/\mathrm{d}s$ is tangential to the centre line of the fibril and perpendicular to the cross-section, while the vectors $d_1(s)$ and $d_2(s)$ lie in the cross sectional plane. This local body coordinate system evolves with s according to $\dot{d}_i(s)/\mathrm{d}s = k(s) \times d_i(s)$, $i = 1, 2, 3$ where $\dot{} = d/\mathrm{d}s$, and the vector of strains $k(s)$ has three components: $\kappa_1(s)$, $\kappa_2(s)$ are the curvatures in the principal directions $d_1(s)$, $d_2(s)$ while $\kappa_3(s) = \tau(s)$ is the twist density. The components of $k(s)$ are most conveniently

‡ Inextensibility and unshearability of fibrils is justified here because the ratio of bending (and twisting) stiffness to stretching (and shearing) stiffness scales with fibril's aspect ratio as $(r/L)^2$, where r is the cross-sectional radius and $L \gg r$ is the fibril length.

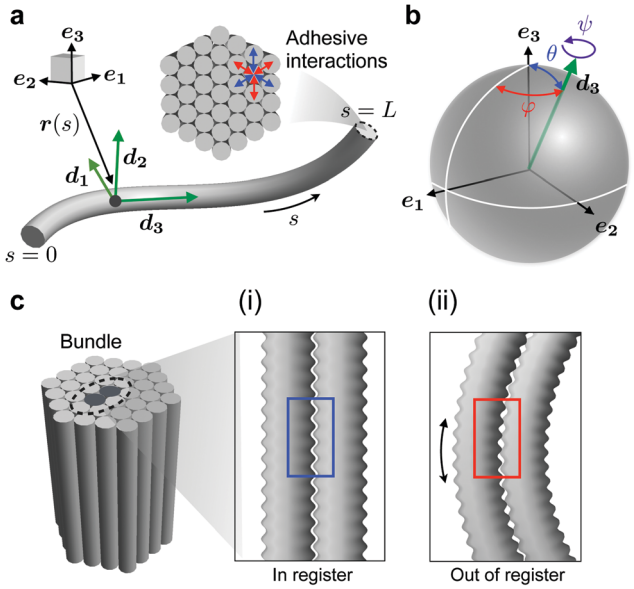

Fig. 2 Mechanical model for the morphology of fibrillar bundles. (a) A fibril is an ordered bundle of a number of filaments linked together by adhesive interactions (inset). To describe bending and twisting modes, we model the fibril as a thin elastic rod with centre line $r(s)$ and homogeneous cross-section. Bending and twisting are then described by a local body reference system attached to each point $s \in [0,L]$ along the fibril length: $d_3(s)$ points tangentially along the fibril's centre line, while $d_1(s)$, $d_2(s)$ point along the principal axes of the fibril. (b) At each point s, the Euler angles θ, φ, ψ describe the rotation of the vectors d_i relative to the fixed reference frame e_i, $i = 1, 2, 3$. (c) Schematic representation of the bending of two adhering inextensible corrugated filaments to illustrate the nature of the adhesive energy term: (i) when the two filaments are straight, the corrugations are in register; (ii) inextensibility of the filaments causes corrugations of bent adhering filaments to be out of registry. Adhesion energy penalises corrugation mismatch between adhering filaments accumulated along the fibril's length and it is minimal when all corrugations are fully in register.

parameterised in terms of the Euler angles θ, ψ, φ, which are defined in Fig. 2(b), as[46]

$$\kappa_1 = \dot{\varphi}\sin\theta\sin\psi + \dot{\theta}\cos\psi, \tag{1a}$$

$$\kappa_2 = \dot{\varphi}\sin\theta\cos\psi - \dot{\theta}\sin\psi, \tag{1b}$$

$$\tau = \dot{\psi} + \dot{\varphi}\cos\theta. \tag{1c}$$

Then the total elastic energy per unit length is written in terms of the strain vector as $\mathscr{H}_{\mathrm{el}} = \frac{B_1}{2}(\kappa_1(s) - \kappa_1^0)^2 + \frac{B_2}{2}(\kappa_2(s) - \kappa_2^0)^2 + \frac{B_3}{2}(\tau(s) - \tau^0)^2$, where $B_1(s)$, $B_2(s)$ are the locally averaged bending rigidities in the directions d_1 and d_2, and B_3 is the locally averaged twisting rigidity. Here κ_1^0, κ_2^0 and τ^0 are spontaneous curvatures and twist that give rise to naturally curved or twisted bundles (Fig. 4(a)). We will initially focus on the case when $\kappa_1^0 = \kappa_2^0 = \tau^0 = 0$ but will come back to naturally curved or twisted bundles in Section 4. Substituting the Euler angle expressions for the curvature and twist, eqn (1), allows us to write the energy density as:[46,47]

$$\mathscr{H}_{\mathrm{el}} = \frac{B_1}{2}\left(\dot{\theta}^2 + \dot{\varphi}^2\sin^2\theta\right) + \frac{B_3}{2}(\dot{\psi} + \dot{\varphi}\cos\theta)^2. \tag{2}$$

We note that the potential energy density of the rod (2) is identical to the kinetic energy of a rigid body once we identify arc-length s with time, the angular velocity with the vector of curvatures and twist, and the bending and twisting stiffnesses with the moments of inertia. This is termed the Kirchhoff kinetic analogy,[46,47] which we will see a use for later on.

2.2.2 Adhesion. To the elastic energy of bending and twisting of the fibril, (2), we add the adhesion energy between individual filaments in the bundle. As seen in our discrete rod simulations, this energy contribution originates in the fact that bending and twisting a bundle of inextensible filaments necessarily couples to sliding and deregistration of inter-filament adhesive bonds. The adhesive potential measured in our simulations is a periodic function of the Euler angles θ and φ. The periodicity of the potential is set by the parameter $\chi = 2\pi d/a$, where a is the separation between monomers and d is the distance between adhering filaments.[48] The amplitude of the potential is determined by the strength of adhesion γ.[48] To construct a simple mean-field energy term to capture this behaviour, consider the interaction between adjacent filaments in the bundle. These filaments are inextensible and unshearable chains of discrete monomers that can be described as thin rods with periodic corrugations along their length (Fig. 2(c)). In the absence of bending or twisting, all corrugations are perfectly in register (Fig. 2(c)(i)). However, since filaments are inextensibile, bending (or twisting) the bundle will cause these corrugations to deregister due to the different path lengths traversed by the neighbouring filaments (Fig. 2(c)(ii)). In the continuum limit, the adhesion energy per unit length in its simplest form can be written as:

$$\begin{aligned}\mathscr{H}_{\mathrm{adh}} &= \frac{\gamma_1}{2}\cos(\chi_1\theta) + \frac{\gamma_2}{2}\sin(\chi_1\theta)\cos(\chi_2\varphi)\\ &\quad + \frac{\gamma_3}{2}\sin(\chi_1\theta)\sin(\chi_2\varphi) + \frac{\gamma_4}{2}\sin(\chi_3\psi),\end{aligned} \tag{3}$$

where the parameters γ_i measure the strength of adhesive interactions and we have decomposed (3) into its principal components associated with the different ways in which the filaments in the bundle can be sheared relative to each other at a cross section, assigning different strengths for each component. The adhesive bonds may possess intrinsic asymmetry due to corrugations having different spatial dimensions along and perpendicular to the filament cross section. We allow for this possibility by introducing different periodicities χ_i for each angle. Moreover, we could account for local packings favouring non-straight configurations by introducing in (3) rest angles θ^0, φ^0, ψ^0 with respect to which all angles in the adhesion energy are measured.

We note that the coarse-grained adhesion energy functional given by (3) was not explicitly implemented in the discrete rod simulations. Instead, our discrete simulations consider only Lennard-Jones interactions between the monomers in the filaments and the periodic nature of the adhesion energy potential emerges naturally from these ingredients, giving credence to our simple choice for the adhesion energy above. Intuitively, deregistration between filaments causes monomers

to be further apart, which leads to weaker adhesive interactions locally. Crucially, while a particular functional dependence of the adhesion potential is assumed for concreteness in (3), it is the periodicity, not the specific form that is important in general.

2.2.3 Effective continuum model. The equilibrium shape of fibrils is determined by searching for the configuration with minimal total energy, $\mathscr{E}_{\mathrm{tot}} = \int_0^L (\mathscr{H}_{\mathrm{el}} + \mathscr{H}_{\mathrm{adh}})\mathrm{d}s$, as a solution to the Euler–Lagrange equations. Once the Euler–Lagrange equations associated with $\mathscr{E}_{\mathrm{tot}}$ have been solved, the centre line of the filament, $r(s)$, is constructed from the tangent vector $d_3(s) = (\sin\varphi(s)\sin\theta(s),\ \cos\varphi(s)\sin\theta(s),\ \cos\theta(s))$ using the relationship $d_3(s) = \mathrm{d}r(s)/\mathrm{d}s$. Within the kinetic analogy, the Euler–Lagrange equations associated with eqn (2) and (3) (see Appendix B) give rise to an ''initial-value'' problem, whereby initial conditions, corresponding roughly to the nucleation solution, and mechanical parameters determine the fibril shape. Non-trivial fibril shapes emerge in our model from the competition between 'kinetic energy' (2), associated with bending and twisting, and adhesion energy (3), which favours straight configurations to maintain corrugations in registry. A natural length scale, termed 'adhesion length'[39] emerges from this competition as $\ell_{\mathrm{adh}} = (B/\gamma)^{1/2}$ and thus sets the characteristic size of fibril shape deformations.

3 Naturally straight and untwisted fibril bundles

Before moving towards a phase diagram of the morphologies and transitions therein, we first show some representative shapes that arise from the minimisation procedure outlined above (see ESI† for details). In Fig. 3(a) we show an image of a zig-zag shaped *Limulus polyphemus* (horseshoe crab) acrosome,[17] a 60 μm long bundle of crosslinked actin filaments characterised by a series of almost straight ''arms'' separated by kink-defects, where bending is concentrated, a feature that our mechanical model can reproduce. As another example of natural fibrils, we consider the shape of *Filopodia* fibrils, which are slender protrusive structures that are made of bundles of actin filaments, cross-linked by proteins such as fascin or plastin.[49,50] Fig. 3(b) shows the image of a reconstituted *Filopodia* fibril with complex helical shape reproduced using our mechanical model.[31] Different kinds of helical fibril morphologies are observed also for inorganic and synthetic structures. An important example are multi-walled carbon nanotubes, fibrils composed of several concentric graphene nanotubes. Fig. 3(c and d) show images of two such multi-walled carbon nanotubes with supercoiled helical and zig-zag shape simulated using our mechanical model.[32]

We note that the values for the elastic parameters used to reproduce the fibrillar shapes in Fig. 3 were not determined by using experimentally measured parameters. In fact, while estimates for bending rigidities B are readily available for different fibril systems from the values of persistence lengths ($\ell_{\mathrm{p}} = B/k_{\mathrm{B}}T$) [*e.g.* actin bundles have $\ell_{\mathrm{p}} \simeq 1$ m, *i.e.* $B \simeq 10^{-21}$ N m^2 at room temperature; single-walled carbon nanotubes have $\ell_{\mathrm{p}} \simeq 10$ μm, *i.e.* $B \simeq 10^{-25}$ N m^2 at room temperature, *etc.*], explicit measurements of the strength of adhesion (parameters γ) are not available for these structures. However, we can use the fibril images together with the associated parameters from our simulations to indirectly estimate the strength of adhesive interactions γ. Indeed, a direct prediction from our model is that fibril deformations occur over a characteristic length scale given by $\ell_{\mathrm{adh}} = (B/\gamma)^{1/2}$, the adhesion length, which measures the competition between bending and adhesion energies. Together with values of bending rigidities estimated from persistence lengths, a comparison between the elastocapillary lengths for simulated fibril shapes and the actual size of deformations for real fibril images would thus allow us to estimate the strength of adhesive interactions. We illustrate this idea on the actin bundle in Fig. 3(a). The simulation parameters allow us to express the simulated fibril shape in units of adhesion length (see scale bars in Fig. 3(a), bottom). Comparing the adhesion length of the simulated shape with the actual scale bars in fibril image, yields the estimate $\ell_{\mathrm{adh}} = (B/\gamma)^{1/2} \simeq 10$ μm. Using $B \simeq 10^{-21}$ N m^2, the estimated adhesion length yields an adhesion strength of about $\gamma = 10k_{\mathrm{B}}T$ nm^{-1}. This value is broadly consistent with estimates of adhesion energies from explicit calculations of van der Waals

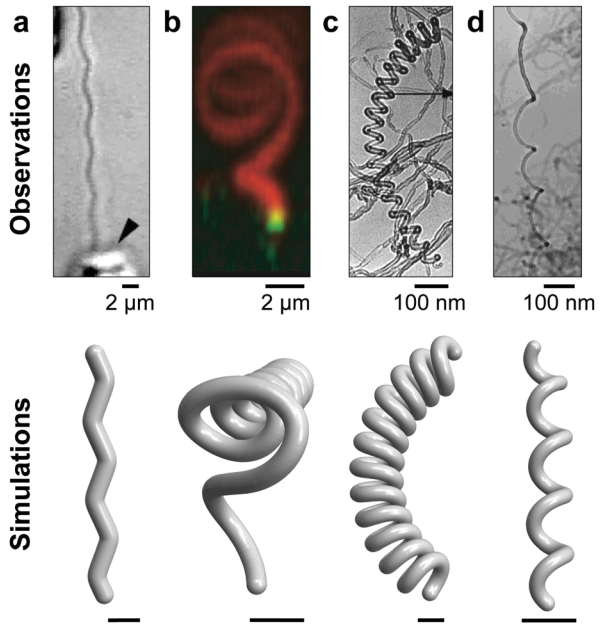

Fig. 3 Examples of natural and synthetic fibrillar morphologies (top) and simulations (bottom) from numerical solution of the Euler–Lagrange equations associated with eqn (2) and (3) (see Appendix B). (a) Image of a zig-zag shaped actin bundle released from the *Limulus polyphemus* sperm.[17,30] (b) Image of a curved *Filopodia*-like structure reconstituted on supported lipid bilayers.[31] (c and d) Tunnel electron microscopy images of multi-walled carbon nanotubes with super-helical and zig-zag morphologies.[32] Scale bars for the simulated shapes correspond to half of the adhesion length $\ell_{\mathrm{adh}} = (B_1/\gamma_1)^{1/2}$; comparing this length scale with the size of observed fibril deformations yields, using bending rigidities determined from persistence lengths, an estimate for the strength of adhesive interactions. For parameters see Appendix B.

attraction between two protein rods obtained using an Hamaker constant for proteins interacting through water are in the order $H_A = 1–10 k_B T$ and distances of closest approach between rods in the nm range.[39]

4 Naturally curved and twisted fibril bundles

Our theory so far has focussed on naturally straight structures. However, fibril bundles can possess spontaneous curvature and/or twist and many biological[8,18,19,29,51–53] and synthetic[11,54–56] filament assemblies are chiral. To account for this fact, we now investigate how the predictions from our model are modified when natural curvatures κ_1^0, κ_2^0 and spontaneous twist τ^0 are introduced in the system (Fig. 4(b), and see Appendix C for the full Hamiltonian and associated Euler–Lagrange equations). We see that $\tau^0 \neq 0$ introduces additional twist to the structure, but does not affect the overall shape of the fibril. This result follows intuition since τ^0 does not break the symmetries associated with the unperturbed Hamiltonian (see Section 5), hence making the predictions of our model applicable to systems with $\tau^0 \neq 0$. By contrast, introducing $\kappa_1^0 \neq 0$ or $\kappa_2^0 \neq 0$ breaks the symmetries of the unperturbed Hamiltonian. This results in helical structures with varying pitch, as expected from a competition between the deformations due to $\ell_{adh} = (B/\gamma)^{1/2}$ and the new natural curvature forced by κ_1^0, κ_2^0. We also observe chiral structures (Fig. 4(c)); fibril bundles of a particular handedness are determined in our model by the sign of the angular momentum ℓ_ψ and can therefore be selected by means of the initial conditions $\dot{\varphi}(0)$ and $\dot{\psi}(0)$. Indeed reversing the sign of $\dot{\varphi}(0)$ and $\dot{\psi}(0)$ (and therefore ℓ_ψ) switches the handedness of the fibril structure from Fig. 3(d).

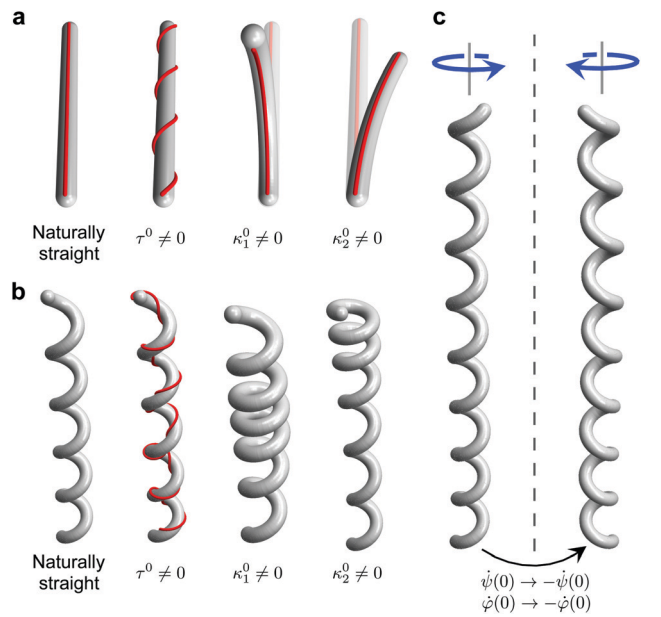

Fig. 4 Naturally curved and twisted fibrillar bundles. (a) Definition of natural curvatures κ_1^0, κ_2^0 and natural twist τ^0. The shapes illustrate a naturally straight fibril (left) and naturally curved or twisted fibrils with $\tau^0 \neq 0$, $\kappa_1^0 \neq 0$ or $\kappa_2^0 \neq 0$. The red line on the fibril shapes indicates the rotation of the tangent $d_3(s)$ along the bundle, hence describing the twist of the fibril. (b) Effect of spontaneous curvatures and twist on the fibril shape of Fig. 3(d). The parameters are the same as for Fig. 3(d) with $\tau^0 = 3$, $\kappa_1^0 = 0.06$ and $\kappa_2^0 = 0.07$, respectively. (c) Emergence of chirality in our model.

5 Phase diagram for fibrillar bundle morphologies

Moving beyond specific morphologies, we now explore systematically the type of fibril shapes that emerge as energy minimizing solutions in our mechanical model as a function of the relevant mechanical parameters. To do so, it is useful to consider the case $\gamma_2 = \gamma_3 = 0$ first and to introduce the terms proportional to γ_2 and γ_3 in eqn (3) as perturbations in a next step, focusing on the case where we have a natural twist $\tau^0 \neq 0$. When $\gamma_2 = \gamma_3 = 0$, the resulting unperturbed Hamiltonian $\mathcal{H}_0$ is independent of φ and ψ. Thus, the associated angular momenta $\ell_\varphi = \partial\mathcal{H}_0/\partial\dot{\varphi}$ and $\ell_\psi = \partial\mathcal{H}_0/\partial\dot{\psi}$ are conserved, and these symmetries allow us to express $\mathcal{H}_0$ in terms of two variables only:

$$\mathcal{H}_0 = \frac{\ell_\theta^2}{2B_1} + \frac{(\ell_\varphi - \ell_\psi \cos\theta)^2}{2B_1 \sin^2\theta} + \frac{\ell_\psi^2}{2B_3} + \frac{\gamma_1}{2}\cos(\chi\theta), \qquad (4)$$

where $\ell_\theta = B_1\dot{\theta}$ and for convenience we have introduced the notation $\chi_1 = \chi$. For $\chi = 1$, eqn (4) may be conveniently recognized as the Hamiltonian describing the configurations of a thin rod with applied load, whose kinetic analogue is the motion of a symmetric rigid body (or a pendulum in two dimensions, $\ell_\varphi = \ell_\psi = 0$) in a gravitational field.[46] Using the kinetic analogy with rigid body dynamics,§ the different fibril morphologies emerging from eqn (4) can be classified into two main classes: (i) precession and nutation modes, where the motion of the polar angle θ remains bounded between some values θ_{min} and θ_{max}, and (ii) libration modes, where the system has sufficient total energy to reach the vertical point $\theta = 0$ and undergo a "tumbling" motion (see Fig. S2, ESI†). Note that, due to the centrifugal term in (4), libration modes are accessible only when $\ell_\varphi = \ell_\psi$, such that we shall assume $\ell_\varphi = \ell_\psi$ throughout. Libration requires the system to have sufficient "kinetic energy", due to bending and twisting, to overcome the potential energy, due to adhesion, a competition that in eqn (4) is described by two natural dimensionless parameters: $\ell_\theta(0)/\sqrt{B_1\gamma_1}$ and $\ell_\varphi/\sqrt{B_1\gamma_1}$. In a phase diagram with these parameters (Fig. 5), moving upwards diagonally corresponds to increasing the ratio of bending and twisting energy ("kinetic energy") to adhesion energy ("potential energy"). Moreover, the homoclinic orbit separates precession and nutation from libration modes. This orbit connects the fixed point $\ell_\theta = 0$ and $\theta = 0$ to itself and, hence, it is the orbit of

§ Note the difference between our model of adhering fibrils and Euler buckling under longitudinal compression: while both models lead to a $\cos\theta$ term in the Hamiltonian, the origin of this term is fundamentally different in the two models. In our model, this term comes from considering the mismatch between adhesion points along the fibril, whereas, in Euler buckling, it is a force density coming from distributing the boundary load among each fibril's cross-section. This analogy therefore does not imply that boundary loading is imposed to the fibril's end in our model.

minimal total energy that is able to librate. In Appendix D we show that a homoclinic orbit exists only if $\ell_\varphi/\sqrt{2B_1\gamma_1} < \chi$ and that this orbit is described by the following equation:

$$\frac{\ell_\theta^2}{B_1\gamma_1} = 1 - \cos(\chi\theta) - \frac{\ell_\varphi^2}{B_1\gamma_1}\frac{(1-\cos\theta)}{(1+\cos\theta)}. \quad (5)$$

Thus, when $\ell_\varphi/\sqrt{2B_1\gamma_1} > \chi$, only librational solutions exist, while for $\ell_\varphi/\sqrt{2B_1\gamma_1} < \chi$, precession and nutation modes are possible, as shown in Fig. 5. The origin corresponds to having zero "kinetic energy" in the Kirchhoff analogy (*e.g.* because initial fibril nucleus starts out straight) or infinite adhesion energy; fibrils will thus remain straight. Precession and nutation modes are characterized by low "kinetic energy" but relatively strong adhesion; the resulting shapes are slightly bent fibrils. Libration modes correspond to structures that have large bending energy (*e.g.* because the fibril nucleus enforces a strong curvature) but relatively low adhesion; the resulting shapes are largely bent fibrils. Interestingly, librating solutions close to the homoclinic orbit are kinked helices that concentrate bending at kinks but are otherwise relatively straight. These solutions maximize the length that is in registry without having to straighten the fibril completely; the cost to pay is the large curvature at the kinks. In the kinetic analogy, kinked helices emerge because these solutions are characterized by points of almost vanishing angular momentum ℓ_θ; thus, if we think of s as a time variable, the system will spend a lot of time in the proximity of these points, but the angle θ in turn changes only very little. As we move away from the homoclinic orbit, solution orbits are characterized by large "kinetic energy" due to bending and twisting and low adhesion energy, such that the kinked character disappears and the cross-section of the helix adopts an increasingly circular shape.

6 Morphological chaos in 3-d fibrillar bundles

We now turn on the terms proportional to γ_2 and γ_3 in eqn (3) and show that this can lead to spatially chaotic solutions, *i.e.* complex spatial configurations for the shape of fibrillar bundles with a very sensitive dependence on the mechanical parameters and initial conditions. The hallmark of chaotic behavior is that small changes in the initial conditions can generate trajectories that deviate from each other significantly (*i.e.* exponentially) over time, which in the context of fibril bundles means that very disparate fibril shapes emerge for very similar initial conditions. The occurrence of spatially chaotic fibril shapes can be thought as a direct implication of Kirchhoff's kinetic analogy. Indeed, it is a well known fact that chaotic dynamics is possible for a spinning top with distinct moments of inertia or for rigid bodies subject to small external torques.[33,34,58] However, it must be stressed that, in the context of the morphology of three dimensional fibrillar bundles, chaotic deformations have a different origin: the components

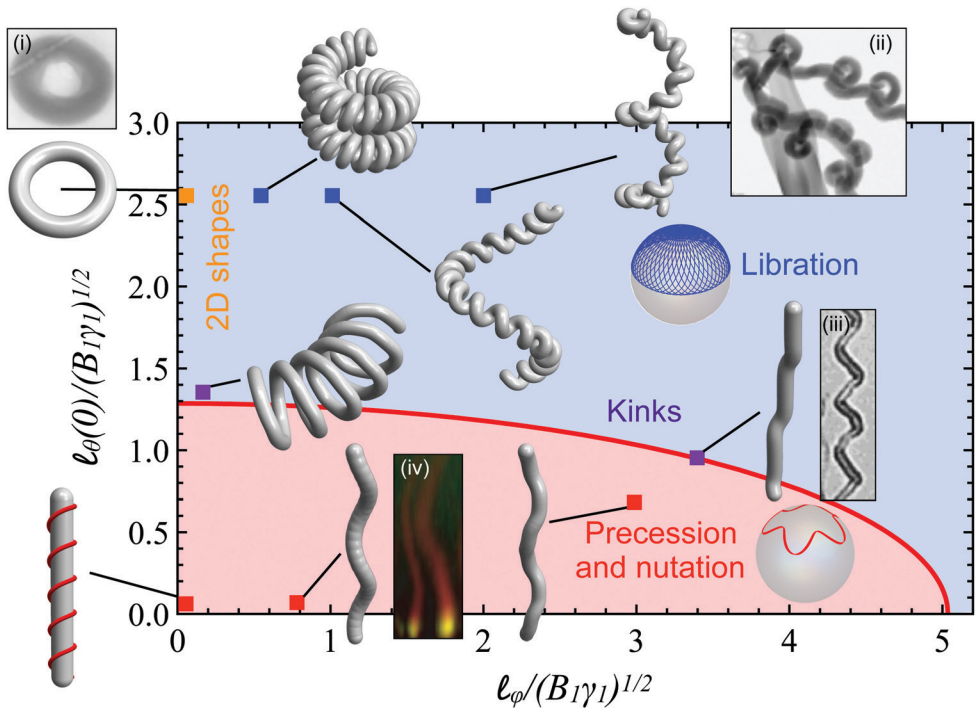

Fig. 5 Phase diagram of fibrillar bundle morphologies. Fibrillar bundle shapes are obtained as energy minimizing solutions from the Hamiltonian eqn (4) as a function of the dimensionless parameters $\ell_\varphi/\sqrt{B_1\gamma_1}$ and $\ell_\theta(0)/\sqrt{B_1\gamma_1}$ for χ = 8, $\theta(0)$ = 0.5 and τ^0 = 2. Fibril shapes are classified as precession and nutation modes (red shaded area) or libration modes (blue shaded area). The boundary line (solid red) is the homoclinic orbit, given in eqn (5). Fibrils near the homoclinic orbit in the libration region are kinked helices (purple); ℓ_φ = 0 corresponds to 2D shapes (orange). The images show comparisons to real fibril systems, including (i and ii) circular and supercoiled carbon nanotubes from,[57] (iii) a kinked carbon nanotube from,[32] and (iv) *Filopodia* structures from.[31] The parameters are listed in Appendix D.

of the adhesion energy perpendicular to the long fibril axis that break the integrability of the full Hamiltonian.¶ The existence of chaotic solutions can be proved in a rigorous manner using the Melnikov integral approach[34,35,58,59] (see Appendix E). The underlying idea of the Melnikov function method is to investigate whether the introduction of terms proportional to γ_2 and γ_3 as perturbations to the fully integrable Hamiltonian system, eqn (4), leads to transverse homoclinic orbits. Transverse homoclinic orbits are distinctive signs of chaotic behavior, which in practice can be tested by establishing whether the Melnikov function has simple zeros. In Appendix E we determine explicitly the Melnikov function for our Hamiltonian and show that this function has simple zeros, therefore indicating the existence of chaotic solutions. This finding may have important implications in the way we think about control in these systems. In particular, tools developed to study complex temporal dynamical systems, such as finite-time and finite-size Lyapunov exponents (FTLE and FSLE),[60] might be deployed to detect spatially chaotic fibril morphologies experimentally. Moreover, different approaches, that have been devised for controlling chaotic systems, including OGY method,[61] may be employed as strategies for achieving morphology control of fibril shapes.

7 Summary and outlook

We have proposed a coarse-grained model to understand the mechanical basis for the shape of three-dimensional fibrillar bundles. Our simulations of adherent filaments in the plane and in space suggest that two basic ingredients naturally define the form of ordered bundles of filaments: intra-filament bending and twisting, and inter-filament adhesion. In terms of these, we derive a Hamiltonian that is analogous to that for a rigid body in an external field and use the Euler–Lagrange equations derived from minimizing it to explain the complex morphologies observed for different natural and synthetic fibrillar bundles. Our phase diagram for the morphologies has a simple interpretation in terms of an analogy to different types of solutions for a spinning rigid body. We also derive a condition for the existence of spatially chaotic morphologies in terms of its nucleation solution. This suggests that regulating the micron-scale shape of three-dimensional self-assembling fibrillar structures is a fundamentally difficult problem, whose solution would require controlling spatial chaos in these systems. With sufficient experimental control on initial conditions (nucleation), a number of self-assembly reactions could be started with slightly different initial conditions to establish how these differences give rise to changes in overall fibril shape. Quantifying the statistics of fibril curvature and torsion from images of fibril shapes, and using this to determine strategies for controlling the shape of three-dimensional fibrillar bundles in space remains an open problem. Although we have demonstrated the existence of chaotic fibril shapes for a specific free energy (eqn (2) and (3)), we note that the flexibility of the Melnikov formalism allows one to include in the future other forms for the energy penalty of geometric frustration in self-assembled fibril bundles.

¶ Note that the adhesion energy (3) breaks the symmetry associated with the conservation of ℓ_φ. The non-integrability of the perturbed Hamiltonian is a necessary condition to give rise to complicated fibril shapes, although this condition is not sufficient for the existence of chaotic behavior, see *e.g.* ref. 62.

Conflicts of interest

There are no conflicts to declare.

A Computer simulations

Simulations begin with an initial seed region consisting of two particles on each filament, enough to establish the initial condition $\theta(0)$. Meanwhile, $\dot{\theta}(0) = \kappa_0$ is prescribed through the intrinsic monomer curvature κ_0 (Fig. 1(a), bottom). To grow the filament, one pair of particles is added at a time, except when a single monomer needs to be added to prevent runaway of one of the filaments relative to the other (see Videos S1 and S2, ESI†). Once added, the pair of monomers is allowed to equilibrate, by trading off between elastic stress and adhesion penalty due to mismatch. During equilibration, only the most recently added pair of monomers and the pair prior to it are mobile, while the rest of the filament is fixed (as – according to the rigid body dynamics analogy – it constitutes the past). The reason the last two pairs of monomers need to be mobile, rather than only the last pair, is to properly model the adhesive interaction, which requires a neighbor on either side.

Each monomer interacts with monomers of the opposite type (*i.e.* on the other fibril) *via* a Lennard-Jones potential with equilibrium distance r_0, and cutoff $2r_0$. The cutoff prevents longer-range interactions, ensuring that the adhesive interaction potential depends only on the local geometry; effectively each monomer only interacts with one or two neighbors on the opposite filament.

Triplets of particles determine a bending interaction, which is mentioned in the main text in the context of a simplified 2d model with φ = const., ψ = const. The bending interaction is simply a discretized bending energy and its general form is analogous to that in the main text, with the 2d angle θ replaced by a 3D angle β: $B/a[1 - \cos(\beta - \beta_0)] \approx B/(2a)(\beta - \beta_0)^2$, where B is the bending rigidity of the fibril, β is the (smaller) angle determined by the segment joining the three consecutive monomers and β_0 is related to the intrinsic curvature κ_0 of the monomers, $\beta_0 = \pi - \kappa_0 a$.

B Euler–Lagrange equations

The Euler–Lagrange equations for eqn (2) and (3) read

$$B_1\ddot{\theta} + (B_3 - B_1)\dot{\varphi}^2 \sin\theta\cos\theta + B_3 \sin\theta\dot{\varphi}\dot{\psi} + \frac{\gamma_1\chi_1}{2}\sin(\chi_1\theta) - \frac{\gamma_2\chi_1}{2}\cos(\chi_1\theta)\cos(\chi_2\varphi) + \frac{\gamma_3\chi_1}{2}\cos(\chi_1\theta)\sin(\chi_2\varphi) = 0, \tag{B1}$$

$$\ddot{\varphi}\left(B_1\sin^2\theta + B_3\cos^2\theta\right) + B_1\dot{\varphi}\dot{\theta}\sin(2\theta) + B_3\left(\ddot{\psi} - \dot{\varphi}\dot{\theta}\sin\theta\right)\cos\theta - B_3(\dot{\psi} + \dot{\varphi}\cos\theta)\sin\theta\dot{\theta} + \frac{\gamma_2\chi_2}{2}\sin(\chi_1\theta)\sin(\chi_2\varphi) - \frac{\gamma_3\chi_2}{2}\sin(\chi_1\theta)\cos(\chi_2\varphi) = 0, \tag{B2}$$

$$B_3(\ddot{\psi} + \ddot{\varphi}\cos\theta - \dot{\varphi}\dot{\theta}\sin\theta) - \frac{\gamma_4\chi_3}{2}\cos(\chi_3\psi) = 0. \tag{B3}$$

These equations are integrated for given initial conditions $\theta(0)$, $\varphi(0)$, $\psi(0)$, $\dot{\theta}(0) = 0$, $\ell_\varphi(0)$ and $\ell_\psi(0)$, where ℓ_φ and ℓ_ψ are the angular momenta with respect to φ and ψ and are given by

$$\ell_\varphi = B_1\sin^2\theta\dot{\varphi} + B_3(\dot{\psi} + \cos\theta\dot{\varphi})\cos\theta, \tag{B4}$$

$$\ell_\psi = B_3(\dot{\psi} + \cos\theta\dot{\varphi}). \tag{B5}$$

The centre line of the fibril $r(s)$ is obtained by integrating the tangent vector

$$d_3(s) = \begin{pmatrix} \sin\varphi(s)\sin\theta(s) \\ \cos\varphi(s)\sin\theta(s) \\ \cos\theta(s) \end{pmatrix} \tag{B6}$$

as $d_3(s) = \mathrm{d}r(s)/\mathrm{d}s$. The twist along the centre line can be followed by means of the vectors

$$d_1(s) = \begin{pmatrix} \cos\varphi(s)\cos\theta(s)\cos\psi(s) - \sin\varphi(s)\sin\psi(s) \\ \sin\varphi(s)\cos\theta(s)\cos\psi(s) + \cos\varphi(s)\sin\psi(s) \\ -\sin\theta(s)\cos\psi(s) \end{pmatrix} \tag{B7}$$

and

$$d_2(s) = \begin{pmatrix} -\cos\varphi(s)\cos\theta(s)\sin\psi(s) - \sin\varphi(s)\cos\psi(s) \\ -\sin\varphi(s)\cos\theta(s)\sin\psi(s) + \cos\varphi(s)\cos\psi(s) \\ \sin\theta(s)\sin\psi(s) \end{pmatrix}. \tag{B8}$$

The parameter used in Fig. 3 are listed here below. In all cases $\theta(0) = \psi(0) = 1$, and $\varphi(0) = -1$. For (a) the parameters were: $\theta(0) = 0.96$, $a = 0.9$, $\beta = 0.9$, $\chi_1 = 4$, and $\gamma_2 = \gamma_3 = 0$, *i.e.* $\ell_{\mathrm{adh}} = \sqrt{B_1/\gamma_1} = 1.05$ (see eqn (D11)). For (b): $\dot{\theta}(0) = 1.3$, $\dot{\varphi}(0) = 1.8$, $B_3\ell_\psi = 2.9$, $B_1 = 1$, $B_3 = 1$, $\gamma_1 = 1.3$, $\gamma_2 = \gamma_3 = 1.3$, $\chi_1 = 2$, $\chi_2 = 3$, $\ell_{\mathrm{adh}} = \sqrt{B_1/\gamma_1} = 0.88$. For (c): $\dot{\theta}(0) = 3.2$, $\dot{\varphi}(0) = 1.9$, $B_3\ell_\psi = 2$, $B_1 = 1$, $B_3 = 1$, $\gamma_1 = 1$, $\gamma_2 = \gamma_3 = 0$, $\chi_1 = 1$, $\ell_{\mathrm{adh}} = \sqrt{B_1/\gamma_1} = 1$. For (d): $\dot{\theta}(0) = 0$, $\dot{\varphi}(0) = 2$, $B_3\ell_\psi = 1$, $B_1 = 1$, $B_3 = 1$, $\gamma_1 = 1$, $\gamma_2 = \gamma_3 = 0$, $\chi_1 = 1$, $\ell_{\mathrm{adh}} = \sqrt{B_1/\gamma_1} = 1$.

C Euler–Lagrange equations for chiral fibrils

For chiral fibrils, we consider the following Hamiltonian with natural curvatures κ_1^0, κ_2^0 and natural twist τ^0

$$\begin{aligned}\mathscr{H} &= \frac{B_1}{2}\left(\dot{\varphi}\sin\theta\sin\psi + \dot{\theta}\cos\psi - \kappa_1^0\right)^2 \\ &+ \frac{B_2}{2}\left(\dot{\varphi}\sin\theta\cos\psi - \dot{\theta}\sin\psi - \kappa_2^0\right)^2 \\ &+ \frac{B_3}{2}\left(\dot{\psi} + \dot{\varphi}\cos\theta - \tau^0\right)^2 + \frac{\gamma_1}{2}\cos\left(\chi_1(\theta - \theta^0)\right) \\ &+ \frac{\gamma_2}{2}\sin\left(\chi_1(\theta - \theta^0)\right)\cos\left(\chi_2(\varphi - \varphi^0)\right) \\ &+ \frac{\gamma_3}{2}\sin\left(\chi_1(\theta - \theta^0)\right)\sin\left(\chi_2(\varphi - \varphi^0)\right) + \frac{\gamma_4}{2}\sin\left(\chi_3(\psi - \psi^0)\right),\end{aligned} \tag{C1}$$

The Euler–Lagrange equations associated with (C1) are

$$\begin{aligned}&-\dot{\varphi}\left(B_1\cos\theta\left(\kappa_1^0\sin\psi + \kappa_2^0\cos\psi\right) - B_3\tau^0\sin\theta + B_3\sin\theta\dot{\psi}\right) \\ &+ (B_1 - B_3)\sin\theta\cos\theta\dot{\varphi}^2 - B_1\left(\dot{\psi}\left(\kappa_1^0\sin\psi + \kappa_2^0\cos\psi\right) + \ddot{\theta}\right) \\ &+ \frac{\chi_1\gamma_1}{2}\sin\left(\chi_1(\theta - \theta^0)\right) - \frac{\chi_1\gamma_2}{2}\cos\left(\chi_1(\theta - \theta^0)\right)\cos\left(\chi_2(\varphi - \varphi^0)\right) \\ &+ \frac{\chi_1\gamma_3}{2}\sin\left(\chi_1(\theta - \theta^0)\right)\sin\left(\chi_2(\varphi - \varphi^0)\right) = 0\end{aligned} \tag{C2}$$

for $\theta(s)$

$$\begin{aligned}&\dot{\theta}\left(-(B_1 - B_3)\sin(2\theta)\dot{\varphi} + B_1\kappa_1^0\cos\theta\sin\psi + B_1\kappa_2^0\cos\theta\cos\psi\right. \\ &\left. - B_3\tau^0\sin\theta + B_3\sin\theta\dot{\psi}\right) + \frac{1}{2}\ddot{\varphi}\left((B_1 - B_3)\cos(2\theta) - B_1 - B_3\right) \\ &+ B_1\sin\theta\dot{\psi}\left(\kappa_1^0\cos\psi - \kappa_2^0\sin\psi\right) - B_3\cos\theta\ddot{\psi} \\ &+ \frac{\chi_2\gamma_2}{2}\sin\left(\chi_1(\theta - \theta^0)\right)\cos\left(\chi_2(\varphi - \varphi^0)\right) \\ &- \frac{\chi_2\gamma_3}{2}\sin\left(\chi_1(\theta - \theta^0)\right)\sin\left(\chi_2(\varphi - \varphi^0)\right) = 0\end{aligned} \tag{C3}$$

for $\varphi(s)$, and

$$\begin{aligned}&\dot{\theta}\left(B_1\kappa_1^0\sin\psi + B_1\kappa_2^0\cos\psi + B_3\sin\theta\dot{\varphi}\right) \\ &- B_1\sin\theta\dot{\varphi}\left(\kappa_1^0\cos\psi - \kappa_2^0\sin\psi\right) - B_3\left(\cos\theta\ddot{\varphi} + \ddot{\psi}\right) \\ &- \frac{\gamma_4\chi_3}{2}\cos\left(\chi_3(\psi - \psi^0)\right) = 0\end{aligned} \tag{C4}$$

for $\psi(s)$.

D Analysis of unperturbed equations

In this appendix we study the solutions that emerge from the unperturbed Hamiltonian:

$$\mathscr{H}_0 = \frac{B_1}{2}\left(\dot{\theta}^2 + \sin^2\theta\dot{\varphi}^2\right) + \frac{B_3}{2}\left(\dot{\psi} + \cos\theta\dot{\varphi} - \tau^0\right)^2 + \frac{\gamma}{2}\cos(\chi\theta), \tag{D1}$$

where for convenience we have introduced the notation $\gamma_1 = \gamma$ and $\chi_1 = \chi$.

D.1 Special limits

The Hamiltonian (D1) has two important limits. When $\chi = 1$, the Hamiltonian (D1) becomes the Hamiltonian of the heavy symmetric top, *i.e.* the motion of a symmetric rigid body around a fixed point under the influence of gravity:

$$\mathscr{H} = \frac{B_1}{2}\left(\dot{\theta}^2 + \sin^2\theta\dot{\varphi}^2\right) + \frac{B_3}{2}(\dot{\psi} + \cos\theta\dot{\varphi})^2 + \frac{\gamma}{2}\cos\theta. \tag{D2}$$

In this analogy, the adhesion potential term corresponds to the gravitational potential, with $\gamma/2 = mg$, where m is the rigid body mass and g is the acceleration due to gravity. Moreover, when $\chi = 1$ and $\dot{\psi} = \dot{\varphi} = 0$, eqn (D1) simplifies to the Hamiltonian describing the motion of a pendulum in the plane with $\hat{\theta} = \pi - \theta$:

$$\mathscr{H} = \frac{B_1}{2}\dot{\hat{\theta}}^2 - \frac{\gamma}{2}\cos\hat{\theta}, \tag{D3}$$

where, in this case, γ/B_1 corresponds to g/L, where L is the length of the pendulum.

D.2 Integration of unperturbed equations

We note that $\mathscr{H}_0$ is independent of φ and ψ, *i.e.* φ and ψ are cyclic variables. Therefore, the angular momenta associated with the angles φ and ψ must be conserved so that

$$\frac{\partial\mathscr{H}_0}{\partial\dot{\psi}} = B_3\left(\dot{\psi} + \cos\theta\dot{\varphi} - \tau^0\right) = \text{const} \equiv \ell_\psi \tag{D4}$$

and

$$\frac{\partial\mathscr{H}_0}{\partial\dot{\varphi}} = B_1\sin^2\theta\dot{\varphi} + B_3\left(\dot{\psi} + \cos\theta\dot{\varphi} - \tau^0\right)\cos\theta = \text{const} \equiv \ell_\varphi. \tag{D5}$$

By combining eqn (D4) and (D5), we find

$$\dot{\varphi} = \frac{\ell_\varphi - \ell_\psi\cos\theta}{B_1\sin^2\theta}. \tag{D6}$$

Using these relationships, we can reduce the Hamiltonian (1) to

$$\mathscr{H}_0 = \frac{\ell_\theta^2}{2B_1} + \frac{(\ell_\varphi - \ell_\psi\cos\theta)^2}{2B_1\sin^2\theta} + \frac{\ell_\psi^2}{2B_3} + \frac{\gamma}{2}\cos(\chi\theta). \tag{D7}$$

where $\ell_\theta = B_1\dot{\theta}$ is the angular momentum in the θ direction. Note that ℓ_θ is not conserved since θ is not a cyclic variable of (D1).

The problem can be simplified further by noticing that the Hamiltonian (D1) does not depend on s explicitly, *i.e.* $\partial\mathscr{H}_0/\partial s = 0$. Hence, $\mathscr{H}_0$ must be equal to a constant for all s:

$$E = \frac{\ell_\theta^2}{2B_1} + \frac{(\ell_\varphi - \ell_\psi\cos\theta)^2}{2B_1\sin^2\theta} + \frac{\ell_\psi^2}{2B_3} + \frac{\gamma}{2}\cos(\chi\theta). \tag{D8}$$

Finally, it is useful to introduce the following new variable $u = \cos\theta$ such that eqn (D8) becomes:

$$E = \frac{B_1}{2}\frac{\dot{u}^2}{1-u^2} + \frac{(\ell_\varphi - \ell_\psi u)^2}{2B_1(1-u^2)} + \frac{\ell_\psi^2}{2B_3} + \frac{\gamma}{2}T_\chi(u), \tag{D9}$$

where $T_\chi(u) = \cos(\chi\theta)$ denotes the Chebyshev polynomial of degree χ. Solving the above equation for $\dot{u}$ yields

$$\dot{u}^2 = [\alpha - \beta T_\chi(u)](1-u^2) - (a - bu)^2 \equiv f(u), \tag{D10}$$

where

$$\alpha = \frac{2E}{B_1} - \frac{\ell_\psi^2}{B_1B_3} \tag{D11a}$$

$$\beta = \frac{\gamma}{B_1} \tag{D11b}$$

$$a = \frac{\ell_\varphi}{B_1} \tag{D11c}$$

$$b = \frac{\ell_\psi}{B_1}. \tag{D11d}$$

Note that, by definition, u is defined only for $-1 \le u \le 1$. Moreover, since the left-hand side of eqn (D10) is non-negative, $\dot{u}^2 \ge 0$, eqn (D10) has a solution only when $f(u) \ge 0$. Under these circumstances, the solution reads

$$s(u) - s(u_0) = \int_{u_0}^{u}\frac{\mathrm{d}u'}{\sqrt{f(u')}}. \tag{D12}$$

From (D12), we can determine, using $u(s) = \cos\theta(s)$, the evolution of the angles $\varphi(s)$ and $\psi(s)$ by means of the following relationships:

$$\dot{\varphi} = \frac{a - bu}{1-u^2}, \quad \dot{\psi} = \frac{\ell_\psi + \tau^0}{B_3} - \frac{u(a-bu)}{1-u^2}. \tag{D13}$$

The parameters used to generate the fibril structures in Fig. 5 are $\ell_\theta(0)/\sqrt{B_1\gamma_1} = 0,\ 0.07,\ 0.7,\ 0.93,\ 1.35,\ 2.55,\ 2.55,\ 2.55,\ 2.55$, respectively, $\ell_\varphi/\sqrt{B_1\gamma_1} = 0,\ 0.8,\ 3,\ 3.5,\ 0.15,\ 0,\ 0.56,\ 1,\ 2$.

D.3 Existence of homoclinic orbits

A homoclinic orbit is an orbit that connects the saddle point $(\theta,\dot{\theta}) = (0,0)$ to itself (starting at $s \to -\infty$ and ending at $s \to \infty$). Because the total energy is conserved, the energy of a homoclinic orbit can be calculated by evaluating (D8) at $(\theta,\dot{\theta}) = (0,0)$, leading to:

$$E = \frac{\ell_\psi^2}{2B_3} + \frac{\gamma}{2}. \tag{D14}$$

Thus, when $\ell_\varphi = \ell_\psi$, the differential equation describing homoclinic orbits reads:

$$\frac{B_1\dot{\theta}^2}{2} + \frac{\ell_\varphi^2(1-\cos\theta)}{2B_1(1+\cos\theta)} + \frac{\gamma}{2}\cos(\chi\theta) = \frac{\gamma}{2}, \tag{D15}$$

or, equivalently,

$$\dot{u}^2 = (1-u)^2\left[\beta\frac{\big(1-T_\chi(u)\big)(1+u)}{1-u} - b^2\right]. \tag{D16}$$

Note that, since the left-hand side of eqn (D16) is non-negative ($\dot{u}^2 \geq 0$), a homoclinic orbit can exist only if also the right-hand side of eqn (D16) is non-negative, *i.e.* if

$$\beta\frac{\big(1-T_\chi(u)\big)(1+u)}{1-u} \geq b^2 \tag{D17}$$

for some subset of $u \in [-1,1]$. Since the maximum of the left-hand side of (D17) on $u \in [-1,1]$ is attained at $u = 1$, it is useful to consider the following identify for Chebyshev polynomials $T_\chi(u)$:

$$\lim_{u\to 1}\frac{1-T_\chi(u)}{1-u} = \chi^2. \tag{D18}$$

eqn (D18) can be proved by using the following explicit formula for $T_\chi(u)$

$$T_\chi(u) = \sum_{k=0}^{[\chi/2]}(-1)^k\binom{\chi}{2k}u^{\chi-2k}\big(1-u^2\big)^k, \tag{D19}$$

where $[\chi/2]$ denotes the integer part of $\chi/2$, and find

$$\begin{aligned}\frac{1-T_\chi(u)}{1-u} &= \frac{1-u^\chi}{1-u} - \sum_{k=1}^{[\chi/2]}(-1)^k\binom{\chi}{2k}u^{\chi-2k}(1-u)^{k-1}(1+u)^k \\ &= \sum_{i=0}^{\chi-1}u^i - \sum_{k=1}^{[\chi/2]}(-1)^k\binom{\chi}{2k}u^{\chi-2k}(1-u)^{k-1}(1+u)^k,\end{aligned} \tag{D20}$$

where in the last step with have used the formula for geometric sums $\sum_{i=0}^{n-1}u^i = (1-u^n)/(1-u)$. Finally, evaluating the above expression at $u = 1$, we find

$$\lim_{u\to 1}\frac{1-T_\chi(u)}{1-u} = \chi + 2\binom{\chi}{2} = \chi + \chi(\chi-1) = \chi^2. \tag{D21}$$

In summary, by using eqn (D18) in eqn (D17) we find that there is an homoclinic orbit only when $2\beta\chi^2 \geq b^2$, *i.e.* when

$$0 \leq \ell_\varphi \leq \chi\sqrt{2B_1\gamma}. \tag{D22}$$

E Melnikov function analysis of perturbed equation and emergence of spatial chaos

In this appendix we investigate the existence of spatial chaos, *i.e.* complex spatial configurations, in the full Hamiltonian. To do so, we will employ the Melnikov function method[59] by treating the terms of the adhesion potential depending on γ_2 and γ_3 as a perturbation of $\mathscr{H}_0$, *i.e.* wee write $\mathscr{H} = \mathscr{H}_0 + \varepsilon\mathscr{H}_1$ where

$$\mathscr{H}_0 = \frac{\ell_\theta^2}{2B_1} + \frac{\big(\ell_\varphi - \ell_\psi\cos\theta\big)^2}{2B_1\sin^2\theta} + \frac{\ell_\psi^2}{2B_3} + \frac{\gamma_1}{2}\cos(\chi_1\theta) \tag{E1}$$

and

$$\mathscr{H}_1 = \frac{1}{2}[\sin(\chi_1\theta)\cos(\chi_2\varphi) + \delta\sin(\chi_1\theta)\sin(\chi_2\varphi)] \tag{E2}$$

with $\delta = \gamma_3/\gamma_2 = \mathcal{O}(1)$.

We have shown that for $0 < \ell_\psi < \chi_1\sqrt{2\gamma_1 B_1}$ the unperturbed Hamiltonian has a hyperbolic saddle point at $(\theta,\ell_\theta) = (0,0)$ and a homoclinic orbit of energy ${\ell_\psi}^2/(2B_3) + \gamma/2$ connecting it to itself. Note that the homoclinic orbit has the following important properties:

- $\pm\theta^{\mathrm{h}}(t)$ are even functions of time, *i.e.* $\pm\theta^{\mathrm{h}}(-t) = \pm\theta^{\mathrm{h}}(t)$;
- $\pm{\ell_\theta}^{\mathrm{h}}(t)$ are odd functions of time, *i.e.* $\pm{\ell_\theta}^{\mathrm{h}}(-t) = \mp{\ell_\theta}^{\mathrm{h}}(t)$.

We now use an extended Melnikov method developed by Holmes and Marsden (formalism in terms of action-angle variables) to investigate the effect of the perturbation around the homoclinic orbit.[34] In this approach, the Melnikov function is defined as:

$$M = \int_{-\infty}^{\infty}\left\{\mathscr{H}_0, \frac{\mathscr{H}_1}{\Omega}\right\}_{(\theta,\ell_\theta)}\mathrm{d}t, \tag{E3}$$

where the integral is evaluated along the homoclinic orbit $(\pm\theta^{\mathrm{h}},\pm\ell_\theta^{\mathrm{h}})$,

$$\{f,g\}_{(q,\ell)} = \frac{\partial f}{\partial q}\frac{\partial g}{\partial \ell} - \frac{\partial f}{\partial \ell}\frac{\partial g}{\partial q}. \tag{E4}$$

denotes the Poisson Bracket and

$$\Omega = \frac{\partial\mathscr{H}_0}{\partial\ell_\varphi} \tag{E5}$$

is the unperturbed angular frequency along the homoclinic orbit. For $\ell_\varphi = \ell_\psi$ and using eqn (E1), the angular frequency Ω reads:

$$\Omega = \frac{\partial\mathscr{H}_0}{\partial\ell_\varphi} = \frac{\ell_\psi}{B_1(1+\cos\theta)} \neq 0. \tag{E6}$$

Hence, along the homoclinic orbit we have:

$$\varphi(t) = \int_0^t\Omega\mathrm{d}\tau + \varphi_0 = \bar{\varphi}(t) + \varphi_0, \tag{E7}$$

where

$$\bar{\varphi}(t) = \int_0^t\Omega\mathrm{d}\tau = \int_0^t\frac{\ell_\psi}{B_1[1+\cos\theta^{\mathrm{h}}(\tau)]}\mathrm{d}\tau. \tag{E8}$$

Note that, since $\cos\theta^{\mathrm{h}}(\tau)$ is an even function of time, it follows from eqn (E8) that $\bar{\varphi}(t)$ is an odd function of time.‖ We will make use of this property later in the calculation.

‖ If $f(t)$ is some even function of time, then the time integral $g(t) = \int_0^t f(s)\mathrm{d}s$ is an odd function of time. In fact, we can write $g(-t) = \int_0^{-t} f(s)\mathrm{d}s = \int_0^t f(-s)(-\mathrm{d}s) = -\int_0^t f(s)\mathrm{d}s = -g(t)$.

The Poisson Bracket in eqn (E3) is evaluated as:

$$\left\{\mathscr{H}_0, \frac{\mathscr{H}_1}{\Omega}\right\}_{(\theta,\ell_\theta)} = \frac{\partial \mathscr{H}_0}{\partial p_\theta}\frac{\partial(\mathscr{H}_1/\Omega)}{\partial \theta}$$
$$= \frac{p_\theta}{2p_\psi}[\chi_1(1+\cos\theta)\cos(\chi_1\theta) - \sin\theta\sin(\chi_1\theta)]$$
$$\times [\cos(\chi_2\varphi) + \delta\sin(\chi_2\varphi)]. \quad \text{(E9)}$$

The Melnikov function, eqn (E3), is thus given by

$$M = \frac{1}{2p_\psi}\int_{-\infty}^{\infty} p_\theta^{\mathrm{h}}\mathscr{W}(\theta^{\mathrm{h}})[\cos(\chi_2\varphi) + \delta\sin(\chi_2\varphi)]\mathrm{d}t, \quad \text{(E10)}$$

where

$$\mathscr{W}(\theta^{\mathrm{h}}) = \chi_1(1+\cos\theta^{\mathrm{h}})\cos(\chi_1\theta^{\mathrm{h}}) - \sin\theta^{\mathrm{h}}\sin(\chi_1\theta^{\mathrm{h}}). \quad \text{(E11)}$$

where φ is given by eqn (E7). To make progress with the integral (E10), we use the following trigonometric identities

$$\cos(\chi_2\varphi) = \cos(\chi_2\bar{\varphi})\cos(\chi_2\varphi_0) - \sin(\chi_2\bar{\varphi})\sin(\chi_2\varphi_0) \quad \text{(E12)}$$

$$\sin(\chi_2\varphi) = \sin(\chi_2\bar{\varphi})\cos(\chi_2\varphi_0) + \cos(\chi_2\bar{\varphi})\sin(\chi_2\varphi_0) \quad \text{(E13)}$$

such that (E10) can be rewritten as:

$$M = \frac{1}{2p_\psi}\left(\int_{-\infty}^{\infty} p_\theta^{\mathrm{h}}\mathscr{W}(\theta^{\mathrm{h}})\cos(\chi_2\bar{\varphi})\mathrm{d}t\right)[\sin(\chi_2\varphi_0) + \delta\cos(\chi_2\varphi_0)]$$
$$+ \frac{1}{2p_\psi}\left(\int_{-\infty}^{\infty} p_\theta^{\mathrm{h}}\mathscr{W}(\theta^{\mathrm{h}})\sin(\chi_2\bar{\varphi})\mathrm{d}t\right)[\cos(\chi_2\varphi_0) - \delta\sin(\chi_2\varphi_0)]. \quad \text{(E14)}$$

We note that $\mathscr{W}(\theta^{\mathrm{h}})$ is an even function of time (recall that θ^{h} is even); thus the term $p_\theta^{\mathrm{h}}G(\theta^{\mathrm{h}})$ is an odd function of time. For this reason, the first term in eqn (E14) vanishes, since the integrand is an odd function of time, and, hence, we can write the Melnikov function in the following form:

$$M = \frac{1}{p_\psi}\left(\int_0^{\infty} p_\theta^{\mathrm{h}}\mathscr{W}(\theta^{\mathrm{h}})\sin(\chi_2\bar{\varphi})\mathrm{d}t\right)[\cos(\chi_2\varphi_0) - \delta\sin(\chi_2\varphi_0)], \quad \text{(E15)}$$

i.e. we find that the Melnikov function is of the form

$$M(\varphi_0) = C[\cos(\chi_2\varphi_0) - \delta\sin(\chi_2\varphi_0)]. \quad \text{(E16)}$$

From this expression it follows that the Melnikov function has infinitely many simple zeros, which is a sign of the fact that the flow associated with the perturbed Hamiltonian displays chaotic behavior.

Acknowledgements

We acknowledge support from the Swiss National Science Foundation (TCTM), and the MacArthur Foundation (LM). L. M. was partially supported by the National Science Foundation under Grant No. DMR-2011754 and DMR-1922321.

Notes and references

1 G. M. Whitesides, J. P. Mathias and C. T. Seto, *Science*, 1991, **254**, 1312.
2 D. A. Fletcher and R. D. Mullins, *Nature*, 2010, **463**, 485.
3 R. I. Litvinov and J. W. Weisel, *Matrix Biol.*, 2017, **60–61**, 110.
4 L. G. Tilney and D. J. DeRosier, *Proc. Natl. Acad. Sci. U. S. A.*, 2005, **102**, 18785.
5 F. Chiti and C. M. Dobson, *Annu. Rev. Biochem.*, 2017, **86**, 27.
6 T. P. J. Knowles, M. Vendruscolo and C. M. Dobson, *Nat. Rev. Mol. Cell Biol.*, 2014, **15**, 384.
7 W. A. Eaton and J. Hofrichter, *Adv. Protein Chem.*, 1990, **40**, 63.
8 M. S. Turner, M. Briehl, F. Ferrone and R. Josephs, *Phys. Rev. Lett.*, 2003, **90**, 128103.
9 E. Gazit, *Chem. Soc. Rev.*, 2007, **36**, 1263.
10 R. Mezzenga and P. Fischer, *Rep. Prog. Phys.*, 2013, **76**, 046601.
11 Y. Wang, J. Xu, Y. Wang and H. Chen, *Chem. Soc. Rev.*, 2013, **42**, 2930.
12 S. Mann, *Biomineralization: Principles and Concepts in Bioinorganic Materials Chemistry*, Oxford University Press, 2002.
13 M. Lenz and T. A. Witten, *Nat. Phys.*, 2017, **13**, 110.
14 J. J. McManus, P. Charbonneau, E. Zaccarelli and N. Asherie, *Curr. Opin. Colloid Interface Sci.*, 2016, **22**, 73.
15 S. C. Glotzer and M. J. Solomon, *Nat. Mater.*, 2007, **6**, 557.
16 A. J. Baldwin, *et al.*, *J. Am. Chem. Soc.*, 2011, **133**, 14160.
17 J. H. Shin, L. Mahadevan, G. S. Waller, K. Langsetmo and P. Matsudaira, *J. Cell Biol.*, 2003, **162**, 1183.
18 J. W. Weisel, C. Nagaswami and L. Makowski, *Proc. Natl. Acad. Sci. U. S. A.*, 1987, **84**, 8991.
19 L. Makowski and B. Magdoff-Fairchild, *Science*, 1986, **234**, 1128.
20 A. I. Brown, L. Kreplak and A. D. Rutenberg, *Soft Matter*, 2014, **10**, 8500.
21 S. Cameron, L. Kreplak and A. D. Rutenberg, *Soft Matter*, 2018, **14**, 4772.
22 Y. K. Murugesan, D. Pasini and A. D. Rey, *J. Renewable Mater.*, 2015, **3**, 56.
23 G. M. Grason and R. F. Bruinsma, *Phys. Rev. Lett.*, 2007, **99**, 098101.
24 G. M. Grason, *Phys. Rev. E: Stat., Nonlinear, Soft Matter Phys.*, 2009, **79**, 041919.
25 C. Heussinger and G. M. Grason, *J. Chem. Phys.*, 2011, **135**, 035104.
26 A. Haddad, H. Aharoni, E. Sharon, A. G. Shtukenberg, B. Kahr and E. Efrati, *Soft Matter*, 2019, **15**, 116.
27 A. B. Harris, R. D. Kamien and T. C. Lubensky, *Rev. Mod. Phys.*, 1999, **71**, 1745.
28 G. M. Grason, *Soft Matter*, 2020, **16**, 1102.
29 A. Kornyshev, D. Lee, S. Leikin and A. Wynveen, *Rev. Mod. Phys.*, 2007, **79**, 943.
30 D. J. DeRosier, L. Tilney and P. Flicker, *J. Mol. Biol.*, 1980, **137**, 375.
31 K. Lee, J. L. Gallop, K. Rambani and M. W. Kirschner, *Science*, 2010, **329**, 1341.

32 R. Gao, Z. L. Wang and S. Fan, *J. Phys. Chem. B*, 2000, **104**, 1227–1234.
33 M. A. Davies and F. C. Moon, *Chaos*, 1993, **3**, 93.
34 P. J. Holmes and J. E. Marsden, *Indiana Univ. Math. J.*, 1983, **32**, 273.
35 V. S. Aslanov, *Int. J. Non-Lin. Mech.*, 2015, **73**, 85.
36 D. M. Hall, I. R. Bruss, J. R. Barone and G. M. Grason, *Nat. Mater.*, 2016, **15**, 727.
37 G. M. Grason, *J. Chem. Phys.*, 2016, **145**, 110901.
38 A. Aggeli, I. Nyrkova, M. Bell, R. Harding, L. Carrick, T. McLeish, A. Semenov and N. Boden, *Proc. Natl. Acad. Sci. U. S. A.*, 2001, **98**, 11857.
39 A. Cohen and L. Mahadevan, *Proc. Natl. Acad. Sci. U. S. A.*, 2003, **21**, 12141.
40 L. Mahadevan, *Faraday Discuss.*, 2008, **139**, 9.
41 H. Aharoni, Y. Abraham, R. Elbaum, E. Sharon and R. Kupferman, *Phys. Rev. Lett.*, 2012, **108**, 238106.
42 I. R. Bruss and G. M. Grason, *Phys. Rev. X*, 2018, **8**, 031046.
43 M. Upmanyu, H. L. Wang, H. Y. Liang and R. Mahajan, *J. R. Soc., Interface*, 2008, **5**, 303.
44 A. K. Buell, *et al.*, *Phys. Rev. Lett.*, 2010, **104**, 228101.
45 H. J. Limbach, A. Arnold, B. A. Mann and C. Holm, *Comput. Phys. Commun.*, 2006, **174**(9), 704–727.
46 A. E. H. Love, *A Mathematical Theory of Elasticity*, Dover, Mineola, NY, 1944, ch. 19.
47 G. Kirchhoff, *J. Math.*, 1859, **56**, 285.
48 D. J. DeRosier, *J. Mol. Biol.*, 1984, **175**, 57.
49 R. W. Davenport, P. Dou, V. Rehder and S. B. Kater, *Nature*, 1993, **361**, 721.
50 B. Lendvai, E. A. Stern, B. Chen and K. Svoboda, *Nature*, 2000, **404**, 876.
51 A. C. Neville, *Biology of Fibrous Composites: Development Beyond the Cell*, Cambridge University Press, Cambridge, 1993.
52 Y. Bouligand, *C. R. Chim.*, 2008, **11**, 281.
53 J. Charvolin and J.-F. Sadoc, *Biophys. Rev. Lett.*, 2014, **9**, 225.
54 W. A. McDade and R. Josephs, *J. Struct. Biol.*, 1993, **110**, 90.
55 S. Che, Z. Liu, T. Ohsuna, K. Sakamoto, O. Terasaki and T. Tatsumi, *Nature*, 2004, **429**, 281.
56 J. F. Douglas, *Langmuir*, 2009, **25**, 8386.
57 A. Shaikjee and N. J. Coville, *J. Adv. Res.*, 2012, **3**, 195.
58 X. Tong and B. Tabarrok, *Arch. Appl. Mech.*, 1996, **66**, 215.
59 V. K. Melnikov, *Transactions of the Moscow Mathematical Society*, 1963, **12**, 1–57.
60 D. Karrasch and G. Haller, *Chaos*, 2013, **23**, 043126.
61 E. Ott, C. Grebogi and J. A. Yorke, *Phys. Rev. Lett.*, 1990, **64**, 1196.
62 A. Mielke and P. Holmes, *Arch. Ration. Mech. Anal.*, 1988, **101**, 319–348.

